

Correlated Nonlinear Phase-Noise in Multi-Subcarrier Systems: Modeling and Mitigation

*Original*

Correlated Nonlinear Phase-Noise in Multi-Subcarrier Systems: Modeling and Mitigation / Golani, Ori; Pilori, Dario; Guiomar, Fernando Pedro Pereira; Bosco, Gabriella; Carena, Andrea; Shtaif, Mark. - In: JOURNAL OF LIGHTWAVE TECHNOLOGY. - ISSN 0733-8724. - ELETTRONICO. - 38:6(2020), pp. 1148-1156. [10.1109/JLT.2019.2939706]

*Availability:*

This version is available at: 11583/2804423 since: 2020-04-14T09:25:54Z

*Publisher:*

IEEE

*Published*

DOI:10.1109/JLT.2019.2939706

*Terms of use:*

This article is made available under terms and conditions as specified in the corresponding bibliographic description in the repository

*Publisher copyright*

IEEE postprint/Author's Accepted Manuscript

©2020 IEEE. Personal use of this material is permitted. Permission from IEEE must be obtained for all other uses, in any current or future media, including reprinting/republishing this material for advertising or promotional purposes, creating new collecting works, for resale or lists, or reuse of any copyrighted component of this work in other works.

(Article begins on next page)

# Correlated nonlinear phase-noise in multi-subcarrier systems: modeling and mitigation

Ori Golani, Dario Pileri, Fernando Pedro Pereira Guiomar, Gabriella Bosco, Andrea Carena, and Mark Shtaif

**Abstract**—In multi-subcarrier wavelength-division-multiplexed (WDM) systems, spectrally close subcarriers are influenced by nonlinearity in a similar way. This causes the nonlinear interference noise (NLIN) that affects them to be correlated — a fact that can be exploited for nonlinearity mitigation. Focusing on the effect of nonlinearity-induced phase noise (NLPN), we find the auto-correlation and cross-correlation functions of the NLPN influencing different subcarriers, and propose a mitigation algorithm that takes advantage of these correlations so as to improve the overall system performance. We validate our results numerically and experimentally.

**Index Terms**—Optical fiber communication, Nonlinear Interference, Time varying inter symbol interference, Nonlinearity mitigation.

## I. INTRODUCTION

**T**he modeling and mitigation of nonlinear interference effects in fiber-optic transmission has been the holy grail of optical communications research almost from its inception [1]–[4]. Particularly challenging in this context, is the treatment of inter-channel nonlinear interference effects, which is the dominant source of nonlinear interference in modern high-channel-count wavelength-division-multiplexed (WDM) systems [5]. Inter-channel interference is imposed on each of the propagating channels by all other channels that are co-propagating with it along the fiber. From the standpoint of an individual channel’s receiver, inter-channel interference manifests itself as noise, because the data carried by the interfering channels is unknown to it [6], [7]. In what follows, we refer to this noise as nonlinear interference noise, or NLIN.

An important aspect that distinguishes inter-channel NLIN from the noise that is generated by optical amplifiers, is the fact that it is characterized by various correlations that can be used for its mitigation. Most notable are correlations between different time-samples of the NLIN affecting a given data-channel [3], [8], and the correlations between the two polarization channels propagating on the same WDM wavelength [9]. These have been studied extensively [10]–[12] and exploited in a variety of reported equalization schemes [13]–[17]. In this paper we focus on a different type of correlations — those that exists between the NLIN processes of different frequency channels. Our goal is to model these correlations analytically, and then to propose a simple equalization scheme that exploits their existence in order to improve performance.

The general idea is illustrated in Fig. 1, where we consider two spectrally close channels (labeled as  $\mathcal{A}$  and  $\mathcal{B}$ ) and a

third channel (labeled as channel  $\mathcal{C}$ ) that is well separated from them in frequency. Owing to chromatic dispersion, all three channels propagate at different group velocities, but while the velocities of channels  $\mathcal{A}$  and  $\mathcal{B}$  are similar (because of the small frequency separation between them), they differ considerably from the group-velocity of channel  $\mathcal{C}$ . Therefore, many of the symbols in channels  $\mathcal{A}$  and  $\mathcal{B}$  are passed by nearly the same symbols of channel  $\mathcal{C}$  in the process of propagation, implying that the contributions of channel  $\mathcal{C}$  to the NLIN affecting channels  $\mathcal{A}$  and  $\mathcal{B}$  will be strongly correlated with one another.

While correlations between different frequency channels are fairly generic, they are particularly important when considering different subcarriers of the same WDM channel in systems using subcarrier multiplexing (SCM), i.e. when each WDM channel is digitally divided into several independently modulated subcarriers.<sup>1</sup> The reason for this is twofold. Firstly, the channel separation between subcarriers is typically smaller than it is between different WDM channels, and hence the correlation between them is stronger. Secondly, since the processing of the different subcarriers is performed by the same receiver, these correlations can be exploited for NLIN mitigation. Systems using SCM have been studied extensively in recent years. One reason for this is the claimed reduction of certain aspects of transceiver complexity [18], [19]. Another reason is that it is the most suitable scheme for implementing the symbol-rate optimization (SRO) procedure, which has been shown to reduce the total NLIN accompanying the signal and increase the system’s maximum-reach [11], [20], [21]. We will characterize the correlations between different frequency subcarriers specifically with respect to the nonlinear phase-noise (NLPN) component of the NLIN. The NLPN is known to be the strongest NLIN component in many cases of interest [22], and particularly so in systems using SCM [23]. The trend of deploying probabilistic shaping in transmission systems is likely to enhance the relative significance of NLPN even further [24], [25].

The paper consists of two major parts. The first (covered in Sec. II) is devoted to the analytical derivation of a model that accurately predicts the correlations between the NLPN processes that affect different subcarrier channels. The model validation is performed numerically (by means of extensive split-step simulations) and experimentally. While the numerical validation clearly demonstrates the model’s accuracy, the agreement with the experimental results is only qualitative.

O. Golani and M. Shtaif are with the School of Electrical Engineering, Tel Aviv University, Tel Aviv, Israel 69978. D. Pileri, A. Carena, and G. Bosco are with DET, Politecnico di Torino, 10129 Torino, Italy. F. Guiomar is with Instituto de Telecomunicações, Aveiro, Portugal.

Manuscript received April XX, 2019; revised XXX yy, 2019.

<sup>1</sup>We should clarify that the derivation performed in this paper also applies to other scenarios, such as system using OFDM or WDM super-channels, but our examples will only focus on SCM transmission, where the phenomena that we explore are strongest.

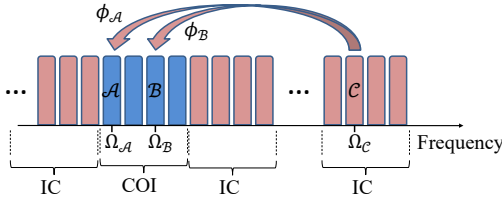


Fig. 1. Schematic description of NLPN generation in an SCM scheme. The NLPN processes  $\phi_A$  and  $\phi_B$  that are imposed on the subcarriers  $\mathcal{A}$  and  $\mathcal{B}$  of the channel of interest (COI) are produced by the nonlinear interference generated by subcarrier  $\mathcal{C}$  of a well separated interfering channel (IC).

The reason for the difficulty of achieving a close quantitative match between the experiment and the theory (or the experiment and the simulation) follows from the presence of laser phase-noise in the experiment and from the fact that the experiment inevitably deploys equalization mechanisms (for phase and polarization recovery) whose modeling is outside the scope of our current work. Nonetheless, the qualitative behavior that is predicted by the theory is clearly evident in the experimental results. In the second part of the paper (covered in Sec. III), we examine the usefulness of the correlations between different subcarriers for the purpose of NLIN mitigation. This is done by means of an adaptive equalization algorithm that is based on a modification of the well-known Wiener filter, which exploits the correlations between different subcarriers. The equalization gain is characterized over a broad range of system parameters, and is demonstrated both numerically (with split-step simulations) and experimentally.

## II. MODELING NLPN

Our goal in this section is to characterize the correlation between the NLPN processes imposed on two different subcarriers (labeled by the indices  $\mathcal{A}$  and  $\mathcal{B}$ ) of the channel of interest (COI), by an interfering subcarrier (labeled by the index  $\mathcal{C}$ ) that belongs to a different WDM channel<sup>2</sup>. In the framework of the first-order perturbation theory, the NLIN that is imposed by the interferer  $\mathcal{C}$  on the  $n$ -th symbol of  $\mathcal{A}$  can be written as [3], [26],

$$\begin{pmatrix} \tilde{a}_x^{(n)} \\ \tilde{a}_y^{(n)} \end{pmatrix} = \left(1 + i\phi_{\mathcal{A}}^{(n)}\right) \begin{pmatrix} a_x^{(n)} \\ a_y^{(n)} \end{pmatrix} + \begin{pmatrix} w_{\mathcal{A},x}^{(n)} \\ w_{\mathcal{A},y}^{(n)} \end{pmatrix}, \quad (1)$$

where  $a_x^{(n)}$  and  $a_y^{(n)}$  are the two polarization components of the  $n$ -th data symbol,  $\phi_{\mathcal{A}}^{(n)}$  is the (time-varying) NLPN component affecting the  $n$ -th symbol, and  $w_{\mathcal{A},x}^{(n)}$  and  $w_{\mathcal{A},y}^{(n)}$  account for nonlinear noise due to processes that do not manifest themselves as NLPN. A similar equation can be written for subcarrier  $\mathcal{B}$ ,

$$\begin{pmatrix} \tilde{b}_x^{(n)} \\ \tilde{b}_y^{(n)} \end{pmatrix} = \left(1 + i\phi_{\mathcal{B}}^{(n)}\right) \begin{pmatrix} b_x^{(n)} \\ b_y^{(n)} \end{pmatrix} + \begin{pmatrix} w_{\mathcal{B},x}^{(n)} \\ w_{\mathcal{B},y}^{(n)} \end{pmatrix}, \quad (2)$$

where the meaning of the symbols relating to subcarrier  $\mathcal{B}$  is self explanatory. We note that the effect of amplification noise

<sup>2</sup>The same derivation also hold if subcarrier  $\mathcal{C}$  belongs to the same WDM channel as  $\mathcal{A}$  and  $\mathcal{B}$ , but in this case the treatment of the NLPN as noise is less warranted, as it could be regarded as a deterministic effect with respect to the COI, and mitigated by means such as digital back propagation.

is immaterial within the framework of the current analysis and therefore it is not included in Eqs. (1) and (2). As demonstrated in [3], the NLPN processes  $\phi_{\mathcal{A}}$  and  $\phi_{\mathcal{B}}$  are given by

$$\phi_{\mathcal{A}}^{(n)} = \frac{3}{2} \sum_{h,k} X_{h,k,0}^{(\mathcal{A})} \left( c_x^{(k+n)*} c_x^{(h+n)} + c_y^{(k+n)*} c_y^{(h+n)} \right) \quad (3)$$

$$\phi_{\mathcal{B}}^{(n)} = \frac{3}{2} \sum_{h,k} X_{h,k,0}^{(\mathcal{B})} \left( c_x^{(k+n)*} c_x^{(h+n)} + c_y^{(k+n)*} c_y^{(h+n)} \right), \quad (4)$$

where  $c_x^{(n)}$  and  $c_y^{(n)}$  denote the two polarization components of the  $n$ -th data-symbol of  $\mathcal{C}$ , and  $X_{h,k,0}^{(\mathcal{A})}$ ,  $X_{h,k,0}^{(\mathcal{B})}$  are a set of interaction coefficients that are independent of the transmitted data and determined only by the link structure, the fundamental waveforms used by the various subcarriers, and the frequency separation between them [27].

Notice that the only difference between Eqs. (3) and (4) is in the coefficients  $X_{h,k,0}^{(\mathcal{A})}$  and  $X_{h,k,0}^{(\mathcal{B})}$ , and hence as long as these coefficients are closely related to one another, a strong correlation between the two NLPN processes is expected. Physically, the coefficients  $X_{h,k,0}^{(\mathcal{A})}$  and  $X_{h,k,0}^{(\mathcal{B})}$  represent the strength of the nonlinearity and account for the effect of walk-off due to the dispersion and the frequency difference between the interfering subcarriers. Therefore, one can expect them to be similar when the frequency separation between  $\mathcal{A}$  and  $\mathcal{B}$  is much smaller than the frequency differences between  $\mathcal{A}$  and  $\mathcal{C}$  or between  $\mathcal{B}$  and  $\mathcal{C}$ .

### A. Calculating the statistical properties of NLPN

The goal of this section is to describe the 2nd order statistics characterizing the NLPN component, which consists of the auto-covariance functions (ACF) and the cross-covariance functions (CCF) of  $\phi_{\mathcal{A}}^{(n)}$  and  $\phi_{\mathcal{B}}^{(n)}$ . While the derivation of auto-covariances has been described in [3], the cross-covariance functions are described in what follows.

The CCF of  $\phi_{\mathcal{A}}^{(n)}$  and  $\phi_{\mathcal{B}}^{(n)}$  is defined as

$$C_{\phi_{\mathcal{A}},\phi_{\mathcal{B}}}[\Delta n] = \mathbb{E} \left[ \phi_{\mathcal{A}}^{(n)} \phi_{\mathcal{B}}^{(n+\Delta n)} \right] - \mathbb{E} \left[ \phi_{\mathcal{A}}^{(n)} \right] \mathbb{E} \left[ \phi_{\mathcal{B}}^{(n)} \right], \quad (5)$$

where  $\mathbb{E}[\cdot]$  represents the ensemble expectancy operation. Using the machinery and methods detailed in Appendix A of [3], this can be rewritten as

$$C_{\phi_{\mathcal{A}},\phi_{\mathcal{B}}}[\Delta n] = \frac{9}{4} P^2 \left( S_1^{A,B}[\Delta n] + (M-2) S_2^{A,B}[\Delta n] \right), \quad (6)$$

where  $P$  is the launch power of channel  $\mathcal{C}$ ,  $M = \mathbb{E}[|c|^4]/\mathbb{E}[|c|^2]^2$  is the normalized kurtosis of channel  $\mathcal{C}$ 's constellation, and

$$S_1^{A,B}[\Delta n] = \sum_{h,k} X_{h,k,0}^{(\mathcal{A})} X_{h+\Delta n,k+\Delta n,0}^{(\mathcal{B})*} \quad (7)$$

$$S_2^{A,B}[\Delta n] = \sum_k X_{k,k,0}^{(\mathcal{A})} X_{k+\Delta n,k+\Delta n,0}^{(\mathcal{B})*} \quad (8)$$

The values of the summations  $S_1^{A,B}[\Delta n]$  and  $S_2^{A,B}[\Delta n]$  can be found using numerical integration. They are given by

$$S_1^{A,B}[\Delta n] = \frac{1}{(2\pi)^4 T^2} \iint_{-\infty}^{\infty} e^{-i\frac{2\pi}{T}\omega\Delta n} I_{A,0,0}(\omega, \omega'') \sum_{h,k} I_{B,h,k}^*(\omega, \omega'') d\omega d\omega'', \quad (9)$$

and

$$S_2^{A,B}[\Delta n] = \frac{1}{(2\pi)^5 T} \int_{-\infty}^{\infty} e^{-i\frac{2\pi}{T}\omega\Delta n} J_{A,0}(\omega) \sum_k J_{B,k}^*(\omega) d\omega, \quad (10)$$

where the functions  $J_{A,k}(\omega)$  and  $I_{A,k,h}(\omega, \omega'')$  are

$$J_{A,k}(\omega) = \int_{-\infty}^{\infty} d\omega' g^*(\omega') g(\omega + \omega' - \frac{2\pi}{T}k) \cdot \int_{-\infty}^{\infty} d\omega'' g^*(\omega'') g(\omega'' - \omega + \frac{2\pi}{T}k) \quad (11)$$

$$\cdot f\left(\left(\omega - \frac{2\pi}{T}k\right)\left(\omega + \omega' - \omega'' - \frac{2\pi}{T}k + \Omega_A - \Omega_C\right)\right) \\ I_{A,k,h}(\omega, \omega'') = g^*\left(\omega'' - \frac{2\pi}{T}k\right) g\left(\omega'' - \omega - \frac{2\pi}{T}h\right) \cdot \int_{-\infty}^{\infty} d\omega' g^*(\omega') g\left(\omega + \omega' - \frac{2\pi}{T}(k+h)\right) \cdot f\left(\left(\omega - \frac{2\pi}{T}(k+h)\right)\left(\omega + \omega' - \omega'' - \frac{2\pi}{T}h + \Omega_A - \Omega_C\right)\right), \quad (12)$$

where  $g(\omega)$  is the subcarriers' spectral shape,  $T$  is the symbol duration, and  $\Omega_A$ ,  $\Omega_B$ , and  $\Omega_C$  are the central angular frequencies of subcarriers  $A$ ,  $B$ , and  $C$ , respectively. The function  $f(u)$  can be referred to as the 'link function' as it describes the accumulated effect of nonlinearity, dispersion, and the link's gain/loss profile. It is defined as

$$f(u) = \int_0^{L_{\text{tot}}} \gamma(z) h(z) e^{id(z)u} dz, \quad (13)$$

where  $\gamma(z)$  is the nonlinear coefficient at point  $z$  along the link,  $h(z)$  describes the gain/loss profile,<sup>3</sup>  $d(z)$  is the accumulated dispersion from the fiber's input to point  $z$ , and  $L_{\text{tot}}$  is the total link length. In the common case of a link composed of  $N$  identical spans of fiber using lumped amplification, Eq. (13) reduces to

$$f(u) = \gamma \frac{1 - e^{(i\beta_2 u - \alpha)L}}{i\beta_2 u - \alpha} \cdot \frac{e^{i\beta_2 uNL} - 1}{e^{i\beta_2 uL} - 1}, \quad (14)$$

where  $L$  is the span length,  $\alpha$  is the loss coefficient,  $\beta_2$  is the chromatic dispersion coefficient, and  $\gamma$  is the nonlinearity coefficient.

Looking at Eq. (6), one can observe an interesting property. The modulation format affects not only the NLPN's variance, but also the shapes of its cross-correlation functions. In general, modulation formats with higher kurtosis values will be characterized by longer correlation times and stronger correlations between different subcarriers, compared to those with a lower kurtosis, as observed in [28].

<sup>3</sup>In the case of lumped amplification  $h(z)$  is a decaying exponential when  $z$  is within the fiber span with jumps at the amplifier locations.

TABLE I  
PHYSICAL SYSTEM PARAMETERS

	Simulations	Experiments
Loss coefficient, $\alpha$	0.2 dB/km	0.162 dB/km
Dispersion coefficient, $\beta_2$	-21.27 ps <sup>2</sup> /km	-25.9 ps <sup>2</sup> /km
Nonlinear coefficient, $\gamma$	1.3 (W · km) <sup>-1</sup>	1.3 (W · km) <sup>-1</sup>
Baud-rate	32/ $N_s$ GBaud	24/ $N_s$ GBaud
Channel spacings	50/ $N_s$ GHz	28/ $N_s$ GHz

## B. Numerical validation

In order to estimate the accuracy of the analytical model, we performed a large set of numerical simulations to assess the properties of NLPN. In all of the examples shown in this section, we used 21 polarization-multiplexed WDM channels on a 50-GHz DWDM grid. Each channel was then divided into  $N_s$  subcarriers, each modulated with a 64-QAM constellation, with symbol rate 32/ $N_s$  GBaud and separated by 50/ $N_s$  GHz. As a COI, we picked the central channel in the WDM spectrum. The number of subcarriers  $N_s$ , was 1, 2, 4 and 8. The link consisted of identical 100-km spans of SMF ( $\alpha = 0.2$  dB/km,  $\beta_2 = -21.27$  ps<sup>2</sup>/km,  $\gamma = 1.3$  (W · km)<sup>-1</sup>, without polarization mode dispersion), separated by amplifiers that fully compensate for the span loss. These parameters are summarized in table I. Fiber propagation is emulated using a GPU-assisted implementation of the split-step Fourier method (SSFM) [29]. Step size was updated according to the nonlinear phase criterion (NLP) [30], with a maximum tolerable nonlinear phase of  $4 \times 10^{-4}$ . The simulation bandwidth was chosen such that the maximum occupied optical bandwidth is not greater than 80% of the simulation bandwidth. The number of spans was set to be between 1 (100 km link) and 20 (2000 km link) so as to provide insight into both short-reach and metro scenarios. The receiver performed electronic dispersion compensation, followed by least mean squares-based adaptive equalization. The equalizer was adaptive only for the first 5500 symbols, afterwards the adaptation was discontinued for the remaining 40960 symbols, in order to avoid any modification of the NLPN statistics.

In order to extract the NLPN  $\phi_{\mathcal{A}}^{(n)}$  for subcarrier  $\mathcal{A}$ , we invert Eq. (1) as follows

$$\frac{1}{2} \left( \frac{\tilde{a}_x^{(n)} - a_x^{(n)}}{a_x^{(n)}} + \frac{\tilde{a}_y^{(n)} - a_y^{(n)}}{a_y^{(n)}} \right) = i\phi_{\mathcal{A}}^{(n)} + w_{\mathcal{A}}^{(n)}, \quad (15)$$

such that  $w_{\mathcal{A}}^{(n)} = \frac{1}{2}(w_{\mathcal{A},x}^{(n)}/a_x^{(n)} + w_{\mathcal{A},y}^{(n)}/a_y^{(n)})$  is a white circular process [10]. We then define our estimate for  $\phi_{\mathcal{A}}^{(n)}$  as

$$\hat{\phi}_{\mathcal{A}}^{(n)} = \frac{1}{2} \text{Im} \left[ \frac{\tilde{a}_x^{(n)} - a_x^{(n)}}{a_x^{(n)}} + \frac{\tilde{a}_y^{(n)} - a_y^{(n)}}{a_y^{(n)}} \right]. \quad (16)$$

An equation equivalent to (15), and an estimator  $\hat{\phi}_{\mathcal{B}}^{(n)}$  for the NLPN of subcarrier  $\mathcal{B}$ , are defined analogously with  $b_{x,y}^{(n)}$  and  $\tilde{b}_{x,y}^{(n)}$  replacing  $a_{x,y}^{(n)}$  and  $\tilde{a}_{x,y}^{(n)}$ , respectively in all places. The quantities  $\hat{\phi}_{\mathcal{A}}^{(n)}$  and  $\hat{\phi}_{\mathcal{B}}^{(n)}$  have the same ACFs and CCF as those of  $\phi_{\mathcal{A}}^{(n)}$  and  $\phi_{\mathcal{B}}^{(n)}$  with the exception of the point  $\Delta n = 0$  in the case of the ACF, where there is a strong contribution

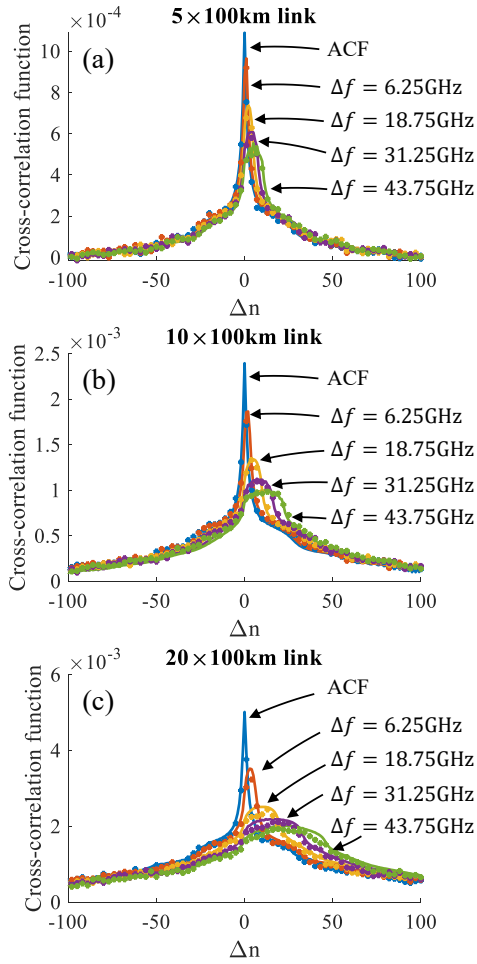


Fig. 2. Cross-correlation functions  $C_{\phi_A, \phi_B}[\Delta n]$ , where subcarrier  $\mathcal{A}$  is chosen to be the lowest-frequency channel within the COI, and subcarrier  $\mathcal{B}$  is placed at a frequency offset of 6.25 GHz (red), 18.75 GHz (yellow), 31.25 GHz (purple), and 43.75 GHz (green). The blue curve corresponds to the ACF of subcarrier  $\mathcal{A}$ ,  $C_{\phi_A, \phi_A}[\Delta n]$ . Results are shown when  $N_s = 8$  for (a)  $5 \times 100$  km link, (b)  $10 \times 100$  km link, and (c)  $20 \times 100$  km link. The launch power was -9 dBm per subcarrier. In all cases, the solid curves correspond to the analytical model and the markers correspond to results obtained using split-step simulations.

of the measurement noise, as observed in [11]. In order to overcome this difficulty, we evaluate the ACFs at  $\Delta n = 0$  by taking advantage of the fact that  $w_{A,B}^{(n)}$  are complex-circular variables, whereas  $\phi_{A,B}^{(n)}$  are real-valued. Hence, we can write for  $\Delta n = 0$

$$C_{\phi_A, \phi_A}[0] = \frac{1}{4} \text{Var} \left[ \text{Im} \left[ \frac{\tilde{a}_x^{(n)} - a_x^{(n)}}{a_x^{(n)}} + \frac{\tilde{a}_y^{(n)} - a_y^{(n)}}{a_y^{(n)}} \right] \right] - \frac{1}{4} \text{Var} \left[ \text{Re} \left[ \frac{\tilde{a}_x^{(n)} - a_x^{(n)}}{a_x^{(n)}} + \frac{\tilde{a}_y^{(n)} - a_y^{(n)}}{a_y^{(n)}} \right] \right], \quad (17)$$

and similarly for the case of  $\phi_B^{(n)}$ . The CCF and the ACFs for values of  $\Delta n \neq 0$  were calculated by replacing  $\phi_{A,B}^{(n)}$  in Eq. (5) by their estimates  $\hat{\phi}_{A,B}^{(n)}$ , and by performing the averaging of the samples in the time domain.

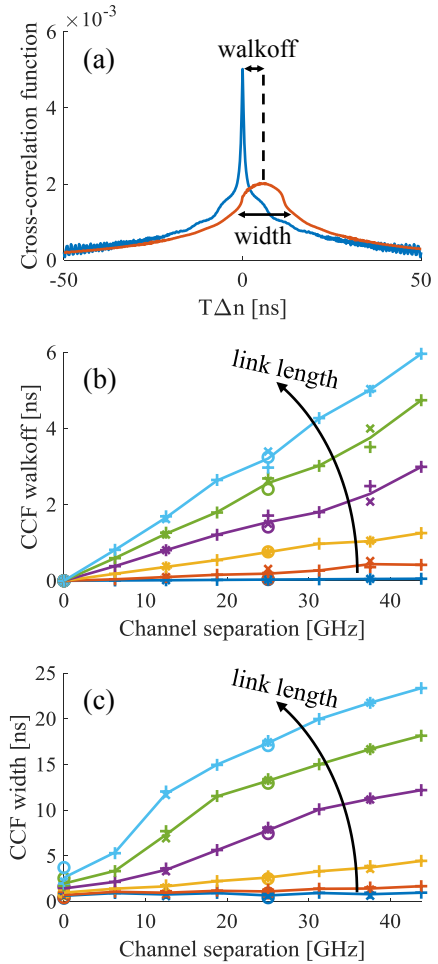


Fig. 3. Walkoff and width of the cross-correlation functions. The CCF's walkoff and width, as a function of link length and subcarrier frequency separation, are shown in (b) and (c), respectively. Results are shown for 100 km, 200 km, 500 km, 1000 km, 1500 km, and 2000 km links, where both the walkoff and width increase monotonically with link length, as indicated by the arrow. The circular (o), cross (x), and plus sign (+) markers correspond to the cases where the channel is divided into 2, 4, and 8 subcarriers, respectively. Note that a channel separation of zero correspond to the ACF of a single subcarrier.

Figure 2 shows the ACFs and the CCFs for the case of  $N_s = 8$  subcarriers, in several link examples. Solid lines correspond to the prediction of the analytical model discussed in the previous section, whereas the markers correspond to the results of split step simulations. The agreement between the model and simulations is self evident. Looking at the curves in Fig. 2, one can observe an interesting characteristic of the CCFs. While the ACFs (blue curves) are, by definition, symmetric and centered around  $\Delta n = 0$ , the CCFs show a significant walkoff of the function's peak location and a broadening of its width. Both the walkoff and the CCF's width increase with the frequency offset between the subcarriers, and with the link length, and both are independent of the launch power. Figure 3 shows the walkoff and width of the CCFs, as a function of the frequency separation between subcarriers. The walkoff is defined as the offset between the maxima of the ACF and the CCF, whereas the width is calculated in a full-width half max (FWHM) sense, i.e. as the point where the

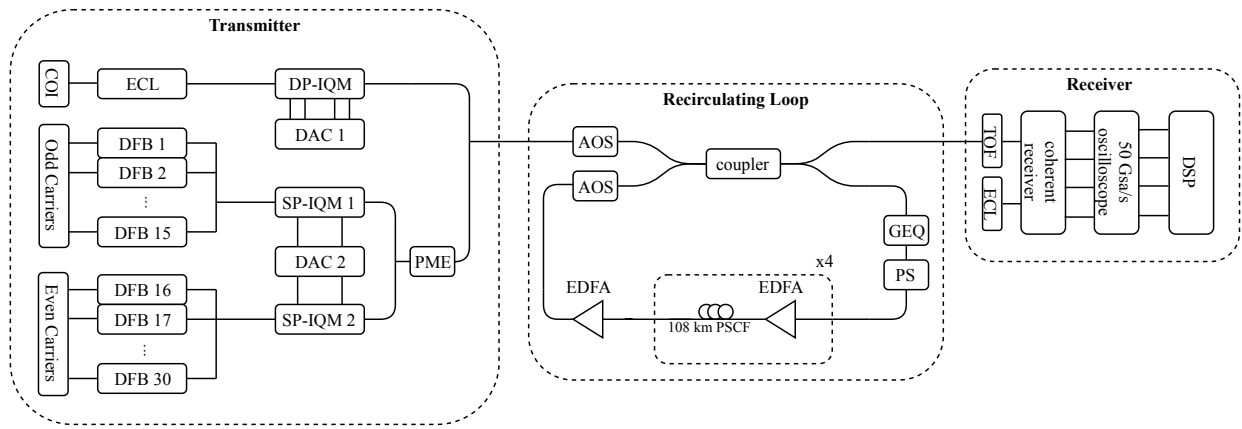


Fig. 4. Experimental setup for subcarrier multiplexing transmission over long-haul distances using a recirculating loop.

CCF drops to half of its maximum value, as illustrated in Fig. 3(a). Both the walkoff and the width are expressed in units of time, i.e. the symbol offset  $\Delta n$  is multiplied by the symbol duration,  $T$ . This allows displaying the results obtained for different values of  $N_s$  on the same curve.

The results for different numbers of subcarriers are practically superimposed on each other. This indicates that both the walkoff and width of the CCFs depend on the frequency separation between the subcarriers, but not on the subcarrier spectral width. Furthermore, the walkoff varies linearly with the frequency separation and the link length. This indicates that the origin of this effect is from the dispersion-induced walkoff between subcarriers.

### C. Experimental demonstration

In addition to the numerical results, the effect of correlated NLPN was demonstrated experimentally. This was done by means of a set of transmission experiments, performed using the recirculating loop setup described in Fig. 4. At the transmitter, the COI is generated in a 4-port digital to analog converter (DAC) at 64 GSa/s and fed to a dual-polarization IQ modulator (DP-IQM), where it modulates the optical carrier provided by an external cavity laser (ECL) with  $<100$  kHz linewidth. Besides the tested channel, 30 additional interfering channels are generated using similar subcarrier multiplexing modulation with uncorrelated data sources. Distributed feedback lasers (DFB) are utilized for the interfering channels, which are grouped into an even-and-odd set of optical carriers and independently modulated in single-polarization IQMs (SP-IQM). A polarization multiplexing emulator (PME) consisting of a 3 dB splitter, optical delay line and polarization beam combiner is then applied to the combined odd and even channels. In order to analyze the impact of NLPN in SCM systems, each of the 31 transmitted channels is then modulated with a varying number of subcarriers,  $N_s \in [1, 2, 4, 6, 8, 12]$ , with a baud-rate of  $24/N_s$  GBaud. All subcarriers are 16-QAM modulated. The recirculating loop is composed of 4 spans of pure silica core fiber (PSCF) with average length of 108 km, dispersion parameter of  $\beta_2 = -25.9$  ps<sup>2</sup>/km and attenuation coefficient of  $\alpha = 0.162$  dB/km. The total span loss, including all insertion losses, is 18.75 dB. We use EDFA

only amplification (noise figure of 5.2 dB) and a spectrally-resolved gain equalizer (GEQ) to compensate for the EDFA gain-tilt and ripples. Finally, a loop synchronized polarization scrambler is used to statistically average the polarization effects. The signal was circulated 4 to 7 times through the loop, which corresponds to transmission distances from 1700 km to 3000 km. At the receiver, the COI was filtered by a tunable optical filter (TOF), mixed with an ECL ( $<100$  kHz linewidth), coherently detected and sampled by a 50 GSa/s real-time oscilloscope (Tektronix DPO73304DX).

The offline digital signal processing (DSP) chain is implemented as follows. First, we perform receiver frontend correction, including Gram-Schmidt orthonormalization, DC removal and IQ deskew. Then, chromatic dispersion is compensated by a frequency-domain zero-forcing equalizer. After frequency recovery through spectral peak detection, the SCM subcarriers are demultiplexed (i.e. filtered and down-converted to baseband). Polarization demultiplexing is performed by a 3-taps  $2 \times 2$  adaptive equalizer driven by the constant modulus algorithm (CMA) over each subcarrier. Carrier phase estimation (CPE) is implemented by the Viterbi & Viterbi algorithm with QPSK partitioning, varying the number of taps between 101 and 1001, in order to study its impact on the overall phase noise auto-correlation. Note that the actual process of phase estimation is applied only over one of the central subcarriers, and then the estimated phase noise is equally removed from all subcarriers. Finally, an  $8 \times 8$  real-valued adaptive equalizer with 51 taps is applied over pairs of frequency-symmetric subcarriers to compensate for the transmitter-side IQ skew [31]. After data-aided convergence, the  $8 \times 8$  equalizer taps are frozen to avoid any impact on the subsequent PPRN mitigation.

Figure 5 shows the measured NLPN cross correlation functions alongside model predictions, for the example of a transmission distance of 3000 km and 8 subcarriers. It is evident that correlated NLPN exists in the experimental data, and that the shape of the measured CCFs is very similar to that of the model predictions. However, unlike the simulation results, we were unable to match the theoretical (or equivalently, the numerical) curves with the experimental ones in a satisfactory quantitative manner. This mismatch is most likely the result

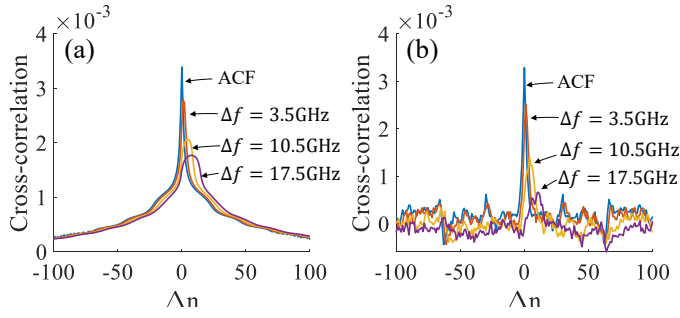


Fig. 5. Comparison of theoretical CCFs (a) and experimentally measured CCFs (b). Results are shown for the case of 8 subcarriers transmitted over 3000 km. The blue curves correspond to the auto-correlation function of the NLPN of a single subcarrier, whereas the red, yellow, and purple curves correspond to the cross-correlation functions between the NLPN affecting subcarriers with a frequency separation of 3.5 GHz, 10.5 GHz, and 17.5 GHz, respectively. The launch power was -8 dBm per subcarrier. For the experimental results, a CPE equalizer with 101 taps was used to mitigate laser phase noise.

of laser phase noise and the CPE algorithm, which are not part of the model and affect the reconstruction of the various correlation functions. The fast-varying NLPN is superimposed on the slow-varying laser phase noise, and cannot be easily differentiated from it. Furthermore, the CPE removes both the laser phase noise and some of the low-frequency components of the NLPN, causing a distortion to the shape of the NLPN's ACFs. This is evident by comparing the sharp peak of the measured ACF (blue curve in Fig. 5b) to the more gradual descent of the theoretical ACF (blue curve in Fig. 5a).

To ascertain that the difference between the model and the experimental results is indeed caused by the laser's line width and the receiver's DSP, we added their effect to the simulations performed in Sec. II-B. Namely, we added ASE and laser phase noise to the received signal, and passed it through the same DSP chain used in the experiment. The laser line width that was used was 100 kHz. Figure 6 shows an example ACF and CCF, with and without the effect of laser phase noise and the receiver's CPE. Much like in the case of the experimental results, the CPE is able to reduce both the laser phase noise and the NLPN, causing the ACF and CCF to be lower, and

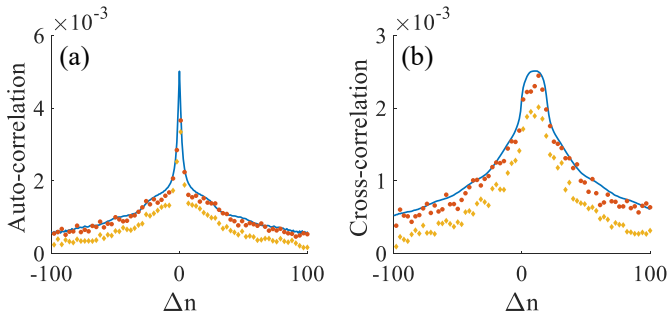


Fig. 6. The effect of laser phase noise and CPE on simulated data. Results are shown for the case of 8 subcarriers transmitted over 2000 km. The ACFs are shown in (a), while (b) shows the CCFs between two subcarriers with a frequency separation of 18.75 GHz. Solid curves correspond to the analytical results, while red circles and yellow diamonds show simulation result with and without the effect of laser phase noise and CPE, respectively.

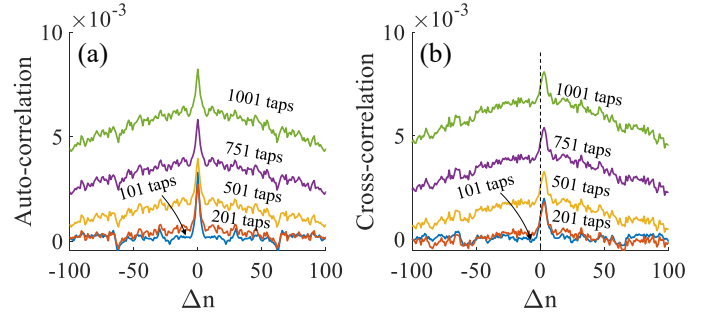


Fig. 7. The effect of the number of taps in the CPE on the measured ACFs (a) and CCFs (b) when  $N_s = 8$ . The CCFs in (b) correspond to a pair of subcarriers that are separated by 7 GHz. The blue, red, yellow, purple, and green curves correspond to 101 CPE taps, 201 taps, 501 taps, 751 taps, and 1001 taps, respectively. In all cases, the launch power was -8 dBm per subcarrier.

with a shorter correlation times.

The effect of the receiver's CPE on the NLPN is further explored in Fig. 7. The CPE's number of taps was varied between 101 and 1001 taps, and the NLPN CCF was measured in each case. Figure 7a shows the ACFs, while Fig. 7b shows the CCF between two subcarriers that are spaced 7 GHz apart. The sharp peaks of the NLPN's ACF and CCF are superimposed on gradually descending CCFs which are caused by the laser phase noise. Increasing the CPE's number of taps simply raises the combined CCFs (NLPN + laser phase noise), but does not affect the shape or position of the NLPN's peak.

### III. JOINT PROCESSING OF SUBCARRIERS FOR PPRN MITIGATION

An important consequence of the existence of correlations between different subcarriers is the potential of exploiting them for the purpose of NLPN mitigation. A simple approach for doing that is explored in the current section. The algorithm, which is described schematically in Fig. 8, is an adaptation of the well known Wiener filter, designed to exploit the estimated CCFs between subcarriers.

Let the received signal of the  $j$ -th subcarrier in time instance  $n$  be  $s_{j,x,y}^{(n)}$ , and let  $D(s_{j,x,y}^{(n)})$  be an estimation of the corresponding transmitted symbol. The algorithm starts by calculating a crude estimation of the NLPN affecting the received signal by using a variation of Eq. (16),

$$\begin{aligned} \tilde{\phi}_j^{(n)} &= \frac{1}{2} \text{Im} \left[ \frac{s_{j,x}^{(n)} - D(s_{j,x}^{(n)})}{D(s_{j,x}^{(n)})} + \frac{s_{j,y}^{(n)} - D(s_{j,y}^{(n)})}{D(s_{j,y}^{(n)})} \right] \\ &= \phi_j^{(n)} + w_j^{(n)}. \end{aligned} \quad (18)$$

Here  $\phi_j^{(n)}$  is the actual value of the NLPN and  $w_j^{(n)}$  is measurement noise. As discussed in [10], this measurement noise is a white additive process, and is caused by the combined contributions of ASE, other components of NLIN (non-phase noise), as well as symbol estimation errors.

In order to clean up the phase estimation and reduce the effect of the measurement noise we implement a filtering procedure which is conducted as follows. First we wish to

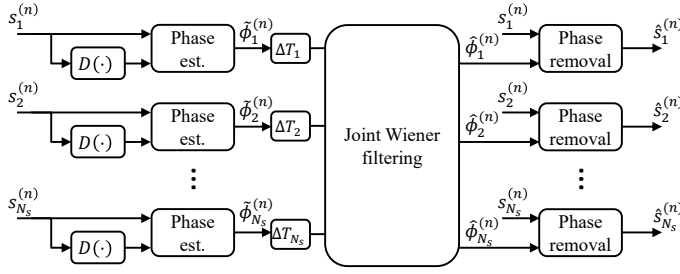


Fig. 8. Block diagram of joint NLPN equalization algorithm.

time-shift the individual subcarriers so that the CCFs between each pair of subcarriers as well as all the ACFs peak at the same position. This is possible owing to the fact that the CCF walkoff depends linearly on channel separation, as can be seen in Fig. 3. Namely, each subcarrier is delayed by an interval  $\Delta T_j$ , where  $j$  is the subcarrier index, and where  $\Delta T_1$  is arbitrarily set to zero. We then construct a vector containing  $N_T$  samples of each of the initial phase estimates,

$$\vec{\phi}^{(n)} = \left( \begin{array}{cccc} \tilde{\phi}_1^{(n-\frac{N_T}{2})} & \dots & \tilde{\phi}_1^{(n+\frac{N_T}{2})} & \dots & \tilde{\phi}_{N_s}^{(n-\frac{N_T}{2})} & \dots & \tilde{\phi}_{N_s}^{(n+\frac{N_T}{2})} \end{array} \right)^T. \quad (19)$$

The parameter  $N_T$  is called the equalizer's number of taps, so that the vector contains  $N_T N_s$  elements.

The discrete finite impulse response (FIR) Wiener filter works by multiplying the vector  $\vec{\phi}^{(n)}$  with a constant matrix, whose structure is determined by the signal's correlation functions and the measurement noise variance [32]. Namely, the estimated phases at time  $n$  are

$$\begin{pmatrix} \hat{\phi}_1^{(n)} \\ \vdots \\ \hat{\phi}_{N_s}^{(n)} \end{pmatrix} = \mathbf{C}_{\vec{\phi}, \phi}^{-1} \mathbf{C}_{\vec{\phi}}^{-1} \vec{\phi}^{(n)}, \quad (20)$$

where  $\mathbf{C}_{\vec{\phi}}$  is the covariance matrix of the vector  $\vec{\phi}^{(n)}$  and  $\mathbf{C}_{\vec{\phi}, \phi}$  is the cross-covariance between  $\vec{\phi}^{(n)}$  and the actual NLPN elements,  $\phi_j^{(n)}$ . As the measurement noise  $w_j^{(n)}$  is uncorrelated with the NLPN elements, the two covariance matrices are

$$\mathbf{C}_{\vec{\phi}, \phi} = \begin{pmatrix} \vec{C}_{1,1} & \dots & \vec{C}_{1,N_s} \\ \vdots & & \vdots \\ \vec{C}_{N_s,1} & \dots & \vec{C}_{N_s,N_s} \end{pmatrix} \quad (21)$$

and

$$\mathbf{C}_{\vec{\phi}} = \sigma_w^2 \mathbb{I} + \begin{pmatrix} \mathbf{C}_{1,1} & \dots & \mathbf{C}_{1,N_s} \\ \vdots & & \vdots \\ \mathbf{C}_{N_s,1} & \dots & \mathbf{C}_{N_s,N_s} \end{pmatrix}, \quad (22)$$

where  $\sigma_w^2$  is the variance of  $w_j^{(n)}$ ,  $\mathbb{I}$  is the unity matrix of size  $N_T N_s \times N_T N_s$ , and  $\vec{C}_{i,j}$ ,  $\mathbf{C}_{i,j}$  are vector and matrix representations of the cross-covariance functions,

$$\vec{C}_{i,j} = (C_{\phi_i, \phi_j}[-\frac{N_T}{2}], \dots, C_{\phi_i, \phi_j}[\frac{N_T}{2}]) \quad (23)$$

and

$$\mathbf{C}_{i,j} = \begin{pmatrix} C_{\phi_i, \phi_j}[0], & C_{\phi_i, \phi_j}[1], & \dots, & C_{\phi_i, \phi_j}[N_T] \\ C_{\phi_i, \phi_j}[-1], & C_{\phi_i, \phi_j}[0], & \dots, & C_{\phi_i, \phi_j}[N_T - 1] \\ \vdots & \vdots & \ddots & \vdots \\ C_{\phi_i, \phi_j}[-N_T], & C_{\phi_i, \phi_j}[1 - N_T], & \dots, & C_{\phi_i, \phi_j}[0] \end{pmatrix}, \quad (24)$$

where  $C_{\phi_i, \phi_j}[\Delta n]$  are the CCFs defined in Eq. (5). The parameters of the Wiener filter can be found either analytically, using the procedure described in Sec. II-A, or from measurements, using the method of Sec. II-B.

The process of NLPN mitigation is implemented by subtracting the estimated phase  $\hat{\phi}_j^{(n)}$  from the received signal  $s_{j,x,y}^{(n)}$ , so that the equalized subcarrier is given by

$$\begin{pmatrix} \hat{s}_{j,x}^{(n)} \\ \hat{s}_{j,y}^{(n)} \end{pmatrix} = e^{-i\hat{\phi}_j^{(n)}} \begin{pmatrix} s_{j,x}^{(n)} \\ s_{j,y}^{(n)} \end{pmatrix}. \quad (25)$$

#### A. Numerical results

The NLPN mitigation algorithm was demonstrated using both the transmission experiments described in Sec. II-C and the simulations described in Sec. II-B. For the simulation, ASE was artificially added at the end of the link, and the EDFA noise figure was set to 5 dB. In the experiments, we used a 101-taps CPE in addition to the NLPN equalization algorithm. In order to observe the added value of using the correlations between subcarriers, we compare the results of the above described joint Wiener filtering to the results obtained when using separate Wiener filtering for the individual subcarriers. In all cases, we use filters with  $N_T = 21$  taps. We found that increasing the number of taps further had a negligible effect on performance.

Figure 9 shows the Q-factor<sup>4</sup> as a function of the launch power for two link examples; a 400 km link using 64-QAM transmission, which is demonstrated using simulations, and a 1700 km link using 16-QAM transmission which was measured experimentally. Notice that without joint Wiener filtering the equalization gain reduces with the number of subcarriers because the temporal correlations within each subcarrier shorten when the number of subcarriers increases, thereby making the NLPN estimation less accurate. In contrast, the equalization gain that is obtained when joint Wiener filtering is applied increases with the number of subcarriers, as expected. This is because more information about the NLPN resides in the cross-correlations between subcarriers when their number increases. Note that the gain in the experimental results is smaller than that obtained in the simulations. The reason for this is that, as argued in Sec. II-C, the receiver's CPE is able to partially compensate for NLPN, leaving less phase noise to be mitigated.

The effect of transmission distance on equalization gain is studied in Fig. 10. In order to provide insight to short reach, metro, and long haul scenarios, we estimated the gain for transmission distances ranging from 200 km to 3000 km. The

<sup>4</sup>The Q factor is defined through the relation  $\text{BER} = \frac{1}{\sqrt{2\pi}} \int_Q^\infty \exp(-x^2) dx$ .

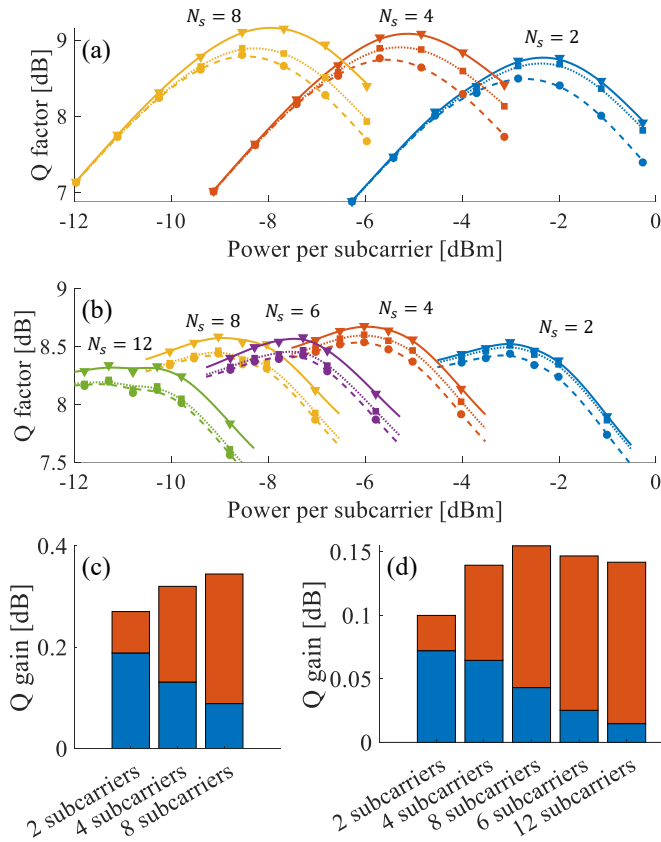


Fig. 9. The gain produced by NLPN equalization. (a) and (b) show Q-factor vs. power curves for different numbers of subcarriers and equalization methods. Simulation results are shown in (a), for the case of a  $4 \times 100$  km link. Experimental results are shown in (b), for the case of a  $16 \times 108$  km link (4 circulations of the recirculating loop setup). The blue, red, purple, yellow, and green curves correspond to  $N_s = 2, 4, 6, 8,$  and  $12$  subcarriers, respectively. Circular markers correspond to the case where no NLPN equalization was used, square markers correspond to the case of disjoint estimation of the NLPN in the various subcarriers, and the triangular markers represent the case of joint estimation of the NLPN. The peak equalization gain (i.e. the difference in the maxima of the Q versus power curves) is shown in (c) and (d), for the simulations and experiments, respectively. The blue bars show the gain from using disjoint NLPN estimation, while the red bars show the added gain from joint estimation of NLPN.

shorter links (less than 1000 km) used 64-QAM modulation and were evaluated using simulations, whereas the longer links (more than 1700 km) used 16-QAM and were measured in experiment. Equalization gains of up to 0.6 dB were reached for the shortest links (200 km), decreasing gradually as the link length is increased. The main reason for the lower performance in longer links is the effect of symbol errors – as the NLPN estimation algorithm is decision-directed, high values of symbol error rates degrade the performance. For this reason, this fairly naive algorithm is likely to be useful in systems utilizing a low-complexity, hard decision forward error correction code (FEC), such as ITU-T G.975.1. In systems with a higher error rate and more complicated soft-decision FECs, one may incorporate the joint-equalization method inside a Turbo-equalization scheme. As shown in [33], [34], incorporating the FEC in the equalization process can be used to achieve performance similar to that of ideal symbol

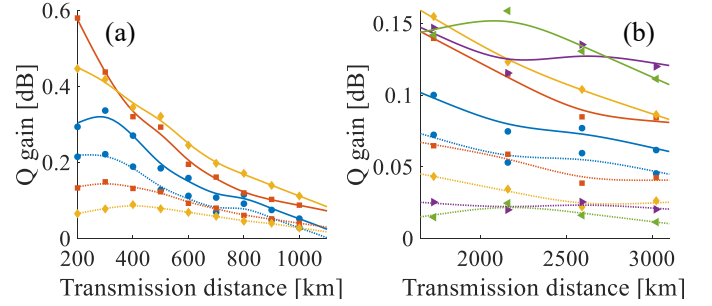


Fig. 10. Equalization gain as a function of the transmission distance. Simulation results are shown in (a), and experimental results in (b). Blue circles correspond to  $N_s = 2$ , red squares to  $N_s = 4$ , purple right-pointing triangles to  $N_s = 6$ , yellow diamonds to  $N_s = 8$ , and green left-pointing triangles to  $N_s = 12$ . Dashed curves show the gain from disjoint NLPN estimation for the various subcarriers, and the solid curves show the gain from joint estimation of the NLPN.

estimation (i.e. without estimation errors). The implementation of such a system is left for future work.

#### B. A quick discussion on complexity

One of the advantages of the proposed joint-processing algorithm is its fairly low computational complexity. As the NLPN is a stationary stochastic process, the covariance matrices of Eq. (20) are constant and their product can be calculated beforehand. This means that at each time instance and for each subcarrier, the algorithm simply takes the scalar product of two  $N_T N_s \times 1$  real-valued vectors (the initial phase estimation,  $\vec{\phi}^{(n)}$ , and a single line of the matrix  $\mathbf{C}_{\vec{\phi}, \vec{\phi}} \mathbf{C}_{\vec{\phi}^{(n)}}^{-1}$ ). The preparation of the initial phase estimation vector,  $\vec{\phi}^{(n)}$ , involves 2 complex multiplications, 3 complex additions, and 2 decision operations, per subcarrier. Note that it is not necessary to calculate the full vector at each time instant. Instead, one can store the phase values of previous steps, calculating only the phase of the latest data point. Lastly, the equalization process itself uses 2 complex multiplications per subcarrier. Assuming that the multiplication operations are the most costly, and that each complex multiplication is equivalent to 4 real-valued multiplications, the overall computational cost, in terms of number of real-valued multiplications, is

$$\text{Cost} = N_T N_s + 16 \quad (26)$$

per dual-polarization symbol per subcarrier.

#### IV. CONCLUSIONS

We have studied the correlations between the NLPN processes added to different frequency channels, and explored the prospects of exploiting these correlations for NLPN mitigation. Our study focused on the particularly relevant case of subcarrier multiplexed systems. When the number of subcarriers is tuned to minimize the NLIN power, it has been shown [11] that the frequency separation between adjacent subcarriers is relatively small (of the order of 3 GHz), in which case we have seen that the correlation between the NLPN affecting different subcarriers is significant. We have shown that this correlation can be used to further reduce the NLPN. While the

performance improvement that our NLPN mitigation method produced was notable, our goal here was only to demonstrate the existence of a potential benefit and not to find an algorithm that maximizes it. The latter problem is left for future work.

We have rigorously derived expressions for the cross-correlation between different frequency channels and demonstrated their validity by comparison with split-step simulations. It should be emphasized that, while we showed results only for the case of subcarrier multiplexed systems, the model is general and applies to other cases, such as OFDM and WDM super-channels.

#### ACKNOWLEDGMENT

The authors are pleased to acknowledge financial support from the Israel Science Foundation Grant 1401/16 and from the Photonext initiative at Politecnico di Torino.

#### REFERENCES

- [1] M. Secondini and E. Forestieri, "On XPM mitigation in WDM fiber-optic systems," *Photonics Technology Letters*, vol. 26, no. 22, pp. 2252–2255, 2014.
- [2] R. Dar, M. Feder, A. Mecozzi, and M. Shtaif, "Pulse collision picture of inter-channel nonlinear interference in fiber-optic communications," *Journal of Lightwave Technology*, vol. 34, no. 2, pp. 593–607, Jan 2016.
- [3] O. Golani, R. Dar, M. Feder, A. Mecozzi, and M. Shtaif, "Modeling the bit-error-rate performance of nonlinear fiber-optic systems," *Journal of Lightwave Technology*, vol. 34, no. 15, pp. 3482–3489, 2016.
- [4] P. Poggiolini, A. Carena, V. Curri, G. Bosco, and F. Forghieri, "Analytical modeling of nonlinear propagation in uncompensated optical transmission links," *Photonics Technology Letters*, vol. 23, no. 11, pp. 742–744, 2011.
- [5] R. Dar and P. J. Winzer, "On the limits of digital back-propagation in fully loaded WDM systems," *Photonics Technology Letters*, vol. 28, no. 11, pp. 1253–1256, 2016.
- [6] P. Poggiolini, G. Bosco, A. Carena, V. Curri, Y. Jiang, and F. Forghieri, "The GN-model of fiber non-linear propagation and its applications," *Journal of Lightwave Technology*, vol. 32, no. 4, pp. 694–721, 2014.
- [7] R. Dar, M. Feder, A. Mecozzi, and M. Shtaif, "Inter-channel nonlinear interference noise in WDM systems: modeling and mitigation," *Journal of Lightwave Technology*, vol. 33, no. 5, pp. 1044–1053, 2015.
- [8] O. Golani, M. Feder, A. Mecozzi, and M. Shtaif, "Correlations and phase noise in NLIN- modelling and system implications," in *Optical Fiber Communication Conference*. Optical Society of America, 2016, p. W3L2.
- [9] M. Winter, C.-A. Bunge, D. Setti, and K. Petermann, "A statistical treatment of cross-polarization modulation in DWDM systems," *Journal of Lightwave Technology*, vol. 27, no. 17, pp. 3739–3751, 2009.
- [10] O. Golani, D. Elson, D. Lavery, L. Galdino, R. Killey, P. Bayvel, and M. Shtaif, "Experimental characterization of nonlinear interference noise as a process of intersymbol interference," *Optics letters*, vol. 43, no. 5, pp. 1123–1126, 2018.
- [11] P. Poggiolini and Y. Jiang, "Recent advances in the modeling of the impact of nonlinear fiber propagation effects on uncompensated coherent transmission systems," *Journal of Lightwave Technology*, vol. 35, no. 3, pp. 458–480, 2017.
- [12] T. Fehenberger, M. Mazur, T. A. Eriksson, M. Karlsson, and N. Hanik, "Experimental analysis of correlations in the nonlinear phase noise in optical fiber systems," in *ECOC 2016; 42nd European Conference on Optical Communication; Proceedings of*. VDE, 2016, pp. 1–3.
- [13] O. Golani, M. Feder, and M. Shtaif, "Equalization methods for out-of-band nonlinearity mitigation in fiber-optic communications," *Applied Sciences*, vol. 9, no. 3, p. 511, 2019.
- [14] —, "Kalman-MLSE equalization for NLIN mitigation," *Journal of Lightwave Technology*, vol. 36, no. 12, pp. 2541–2550, 2018.
- [15] L. Li, Z. Tao, L. Liu, W. Yan, S. Oda, T. Hoshida, and J. C. Rasmussen, "Nonlinear polarization crosstalk canceller for dual-polarization digital coherent receivers," in *Optical Fiber Communication Conference*. Optical Society of America, 2010, p. OWE3.
- [16] M. Secondini, E. Forestieri, and G. Prati, "Achievable information rate in nonlinear WDM fiber-optic systems with arbitrary modulation formats and dispersion maps," *Journal of Lightwave Technology*, vol. 31, no. 23, pp. 3839–3852, 2013.
- [17] T. Fehenberger, M. P. Yankov, L. Barletta, and N. Hanik, "Compensation of XPM interference by blind tracking of the nonlinear phase in WDM systems with QAM input," in *Optical Communication (ECOC), 2015 European Conference on*. IEEE, 2015, pp. 1–3.
- [18] M. Qiu, Q. Zhuge, M. Chagnon, Y. Gao, X. Xu, M. Morsy-Osman, and D. V. Plant, "Digital subcarrier multiplexing for fiber nonlinearity mitigation in coherent optical communication systems," *Optics Express*, vol. 22, no. 15, pp. 18 770–18 777, 2014.
- [19] F. P. Guiomar, L. Bertignono, A. Nespola, and A. Carena, "Frequency-domain hybrid modulation formats for high bit-rate flexibility and nonlinear robustness," *Journal of Lightwave Technology*, vol. 36, no. 20, pp. 4856–4870, Oct. 2018.
- [20] P. Poggiolini, A. Nespola, Y. Jiang, G. Bosco, A. Carena, L. Bertignono, S. M. Bilal, S. Abrate, and F. Forghieri, "Analytical and experimental results on system maximum reach increase through symbol rate optimization," *Journal of Lightwave Technology*, vol. 34, no. 8, pp. 1872–1885, 2016.
- [21] G. Bosco, "Advanced modulation techniques for flexible optical transceivers: the rate/reach tradeoff," *Journal of Lightwave Technology*, vol. 37, no. 1, pp. 36–49, Jan 2019.
- [22] R. Dar, M. Feder, A. Mecozzi, and M. Shtaif, "Properties of nonlinear noise in long, dispersion-uncompensated fiber links," *Optics Express*, vol. 21, no. 22, pp. 25 685–25 699, 2013.
- [23] D. Pilori, F. Forghieri, and G. Bosco, "Residual non-linear phase noise in probabilistically shaped 64-QAM optical links," in *2018 Optical Fiber Communications Conference and Exposition (OFC)*. IEEE, 2018, pp. 1–3.
- [24] J. Cho and P. J. Winzer, "Probabilistic constellation shaping for optical fiber communications," *Journal of Lightwave Technology*, vol. 37, no. 6, pp. 1590–1607, 3 2019.
- [25] F. P. Guiomar, L. Bertignono, A. Nespola, P. Poggiolini, F. Forghieri, and A. Carena, "Combining probabilistic shaping and nonlinear mitigation: Potential gains and challenges," in *Optical Fiber Communication Conference*. OSA, 2018.
- [26] R. Dar, M. Feder, A. Mecozzi, M. Shtaif, and P. J. Winzer, "Nonlinear phase and polarization rotation noise in fully loaded WDM systems," in *ECOC, 2015*, p. P.5.16.
- [27] R. Dar, M. Feder, A. Mecozzi, and M. Shtaif, "Properties of nonlinear noise in long, dispersion-uncompensated fiber links," *Opt. Express*, vol. 21, no. 22, pp. 25 685–25 699, Nov 2013.
- [28] O. Golani, D. Pilori, G. Bosco, and M. Shtaif, "Correlated non-linear phase noise in multi-subcarrier systems," *arXiv preprint*, pp. 1–3, 2018.
- [29] D. Pilori, M. Cantono, A. Carena, and V. Curri, "FFSS: the fast fiber simulator software," in *International Conference on Transparent Optical Networks (ICTON)*. IEEE, 7 2017.
- [30] O. V. Sinkin, R. Holzlohner, J. Zweck, and C. R. Menyuk, "Optimization of the split-step fourier method in modeling optical-fiber communications systems," *Journal of Lightwave Technology*, vol. 21, no. 1, pp. 61–68, 2003.
- [31] G. Bosco, S. M. Bilal, A. Nespola, P. Poggiolini, and F. Forghieri, "Impact of the transmitter IQ-skew in multi-subcarrier coherent optical systems," in *Proc. Optical Fiber Communication Conf. and Exposition (OFC)*, 2016, p. W4A.5.
- [32] R. G. Brown, P. Y. Hwang *et al.*, *Introduction to random signals and applied Kalman filtering*. Wiley New York, 1992, vol. 3.
- [33] O. Golani, M. Feder, and M. Shtaif, "NLIN mitigation using turbo equalization and an extended Kalman smoother," *Journal of Lightwave Technology*, vol. 37, no. 9, pp. 1885–1892, May 2019.
- [34] E. P. da Silva, M. P. Yankov, F. Da Ros, T. Morioka, and L. K. Oxenløwe, "Perturbation-based FEC-assisted iterative nonlinearity compensation for WDM systems," *Journal of Lightwave Technology*, vol. 37, no. 3, pp. 875–881, Feb 2019.